HHS Public Access

Author manuscript

J Magn Reson Imaging. Author manuscript; available in PMC 2019 February 01.

Published in final edited form as:

J Magn Reson Imaging. 2018 February ; 47(2): 554–564. doi:10.1002/jmri.25777.

Nuclei-specific deposits of iron and calcium in the rat thalamus after status epilepticus revealed with quantitative susceptibility mapping (QSM)

Manisha Aggarwal, Ph.D[1,*], **Xu Li, Ph.D**[1,2], **Olli Gröhn, Ph.D**[3], and **Alejandra Sierra, Ph.D**[3]

[1]Russell H. Morgan Department of Radiology and Radiological Science, Johns Hopkins University School of Medicine, Baltimore, MD, USA [2]F. M. Kirby Research Center, Kennedy Krieger Institute, Baltimore, MD, United States [3]A. I. Virtanen Institute for Molecular Sciences, University of Eastern Finland, Kuopio, Finland

Abstract

Purpose—To investigate pathological changes in the rat brain after pilocarpine-induced status epilepticus using quantitative susceptibility mapping (QSM).

Materials and Methods—Three-dimensional (3D) multi-echo gradient-echo (GRE) data were acquired from ex vivo brains of pilocarpine-injected and age-matched control rats at 11.7T. Maps of R2* and quantitative susceptibility were calculated from the acquired 3D GRE magnitude and phase data, respectively. QSM and R2* maps were compared with Perls' (iron) and Alizarin-red-S (calcium) stainings in the same brains to investigate the pathophysiological basis of susceptibility contrast.

Results—Bilaterally-symmetric lesions were detected in reproducible thalamic regions of pilocarpine-treated rats, characterized by hyperintensity in R2* maps. In comparison, quantitative susceptibility maps demonstrated heterogeneous contrast within the lesions, with distinct hyperintense (paramagnetic) and hypointense (diamagnetic) areas. Comparison with histological assessment revealed localized deposits of iron- and calcium-positive granules in thalamic nuclei corresponding to paramagnetic and diamagnetic areas delineated in the susceptibility maps, respectively. Pronounced differences were observed in the lesions between background-corrected phase images and reconstructed susceptibility maps, indicating unreliable differentiation of iron and calcium deposits in phase maps. Multiple linear regression showed a significant association between susceptibility values and measured optical densities (ODs) of iron and calcium in the lesions (R^2=0.42, $p<0.001$), with a positive dependence on OD of iron and negative dependence on OD of calcium.

Conclusion—QSM can detect and differentiate pathological iron and calcium deposits with high sensitivity and improved spatial accuracy compared to R2* or GRE phase images, rendering it a promising technique for diagnosing thalamic lesions after status epilepticus.

[*]**Address correspondence to**: Manisha Aggarwal, Ph.D. Johns Hopkins University School of Medicine, Traylor Building, Room 217, 720 Rutland Avenue, Baltimore, MD 21205, USA, Tel: (+1) 410-502-3553, maggarw@jhu.edu.

Keywords

quantitative susceptibility mapping; R2*; calcification; brain; iron; lesions; epilepsy

INTRODUCTION

Epilepsy can occur as a result of acute brain insults such as traumatic brain injury, cerebral infections, or stroke [1]. Epileptogenesis following such acute insults involves diffuse molecular and cellular changes in the brain that are not yet completely understood. Animal models of pilocarpine- or kainate-induced status epilepticus (SE) are widely used to investigate pathological alterations in the brain underlying epileptogenesis [2,3]. Calcification in the brain has been histologically reported in both the kainate and pilocarpine models of SE [4,5]. Dystrophic calcification or ferrugination is a sequela of brain damage observed in a spectrum of neurological disorders, and is associated with abnormal mineral accumulation in areas of degenerated or necrotic tissue [6]. Although the precise mechanisms of brain tissue mineralization are not currently understood, localized increase in intracellular calcium concentration in areas of apoptotic or necrotic cell death has been proposed to be a primary contributor to calcification [7]. Further, histopathologic evidence at different time points indicates that calcium salt deposits in the rat brain with kainite-induced SE increase in size and concentration over time [4]. Imaging techniques that can allow sensitive and specific detection of mineral deposits in the brain could therefore provide important surrogate markers of regional tissue damage and progression of epileptogenesis.

Currently, computed tomography (CT) is widely used for detection of calcified lesions in the brain. However, CT provides limited soft tissue contrast, and further, calcific or hemorrhagic lesions cannot be effectively distinguished at attenuation levels of <100 Hounsfield units. Quantitative susceptibility mapping (QSM) based on gradient-echo (GRE) signal phase in MRI is differentially sensitive to paramagnetic and diamagnetic effects of variations in tissue molecular composition [8-10], and can therefore potentially provide more specific markers to probe pathological alterations in the brain. Mineralized lesions generate nonspecific signal intensities in conventional spin-echo T2- or T1-weighted sequences, and manifest as hypointense areas in GRE magnitude (T2*-weighted) images. The latter effect stems from the magnetic field perturbation and intravoxel spin dephasing induced by the inhomogeneous magnetic susceptibility distribution of mineralized tissue, which is reflected in the non-local phase of the complex-valued GRE signal [11]. Compared to the water content of most gray matter tissue, iron complexes such as ferritin and hemosiderin are paramagnetic, whereas calcium compounds such as calcium phosphate are diamagnetic.

Previous studies have shown the sensitivity of measured GRE signal phase and associated contrast generated using susceptibility-weighted imaging (SWI) to brain tissue calcification [12,13]. QSM, which solves the ill-posed field-to-source inverse problem, has been used to detect calcifications, microbleeds [14,15], and non-heme iron in the normal brain [16-18] and in neurological disorders [19,20]. More recently, the potential of QSM to differentiate between hemorrhages and calcifications was demonstrated [21,22]. In previous studies in the human brain, CT has been widely used as a reference standard to compare delineation of

calcifications. However, due to the limited sensitivity of CT to detect calcifications at low concentrations, or microbleeds and chronic hemorrhages [21], simultaneous assessment of iron and calcified deposits and their effect on QSM contrast has not been feasible.

In experimental models of epilepsy and traumatic brain injury, well-formed calcifications are usually detected in chronic stages of the disease [23]. Histological studies indicate that in earlier stages, calcium salts may be present in the form of small and diffuse granules [4,5]. Moreover, it is reported that the accumulation of iron tends to precede the deposition of calcium and other minerals in cerebral lesions [24]. Accurate characterization and identification of both the spatial distribution and composition of these lesions could therefore provide key insights into the progression of SE-induced injury and regional pathological changes in epilepsy.

In this study, we set out to investigate pathological changes in the rat brain after pilocarpine-induced SE using QSM based on high-resolution 3D GRE imaging at 11.7 T, and further, to decipher the pathological correlates of magnetic susceptibility alterations in brain lesions after SE using comparison with iron- and calcium-specific histological stainings in the same brains.

MATERIALS AND METHODS

Animals and pilocarpine-induced SE

SE was induced in male Wistar rats (n = 10, 10 weeks old, 300-350 g, National Laboratory Animal Center, Kuopio, Finland). Rats were injected subcutaneously with scopolamine (2 mg/kg, Sigma Chemical Co., St. Louis, MO) to reduce the peripheral adverse effects of pilocarpine. 30 min later, SE was induced by intraperitoneal injection of pilocarpine (320 mg/kg, Sigma Chemical Co.). The development of SE was observed visually for 3 h (by A.S., with 10 years of experience in animal models of epilepsy). Finally, diazepam (10 mg/kg, Stesolid Novum, Dumex-Alpharma, Copenhagen, Denmark) was administered intraperitoneally to reduce mortality. The success rate for producing SE was 80%, and the mortality rate was 37%. Rats that developed recurrent generalized seizures lasting for at least 30 min during the observation period and survived up to three weeks post induction of SE (n = 5) were included in the study. Age-matched control rats (n = 5) were treated similarly but were injected with 0.9% saline solution instead of pilocarpine. At three weeks after induction of status, pilocarpine-injected and age-matched control rats were transcardially perfused with 0.9% saline solution, followed by 4% paraformaldehyde (PFA) in 0.1 M phosphate buffer (30 ml/min; 4°C). The brains were removed from the skulls and immersion-fixed in 4% PFA. All animal procedures were approved by the Animal Ethics Committee of the Provincial Government of Southern Finland and conducted in accordance with the guidelines set by the European Community Council Directives 86/609/EEC.

Data acquisition

MR imaging was performed on a vertical-bore 11.7 T NMR spectrometer (Bruker Biospin, Billerica, MA, USA) equipped with an actively-shielded Micro2.5 gradient system (maximum gradient strength = 1000 mT/m). A 20-mm-diameter birdcage volume coil was

used for radiofrequency transmission and signal reception. Prior to MRI, the brains were transferred to phosphate buffered saline (PBS) for 48 h and then placed in 20-mm-diameter glass tubes which were filled with Fomblin® (Solvay Solexis, Thorofare, NJ, USA) to prevent tissue dehydration and minimize susceptibility distortion near the specimen surface. The brains were positioned with the anterior-posterior axis aligned with the external magnetic field. Before acquisition, Fieldmap based first- and second-order shimming was performed using the MAPshim routine (Bruker Biospin) to optimize B_0 field homogeneity over the brain volume. 3D GRE data of the brains were acquired using a bipolar multi-echo gradient-recalled echo (MGE) sequence with the following imaging parameters: number of echoes = 8, first echo time (TE1) = 5 ms, inter-echo interval (ΔTE) = 5 ms, flip angle 45°, repetition time (TR) = 100 ms, 2 averages, and receiver bandwidth = 70 kHz. The field-of-view (FOV) and matrix size were 16 × 15.4 × 11.6 mm^3 and 132 × 128 × 96, respectively, for a native isotropic resolution of 120 × 120 × 120 μm^3. The total acquisition time was approximately 40 min. Temperature of the specimens was maintained at 36°C during the scans via thermostatically controlled airflow integrated with the spectrometer.

Data reconstruction and analysis

GRE magnitude and phase images were reconstructed from the 3D *k*-space data using in-house written code in IDL6.4 (ITT Visual Systems, Boulder, CO, USA). Complex *k*-space data were apodized by a symmetric 10% trapezoidal function and zero-padded by a factor of two prior to Fourier transformation. R2* maps were calculated by voxel-wise monoexponential fitting of the odd-numbered multi-echo GRE magnitude data with TE. Phase data collected at a TE of 15 ms were used to generate frequency and quantitative susceptibility maps for high signal-to-noise ratio (SNR) and optimal contrast in lesioned areas. Phase maps were first unaliased using a 3D Laplacian-based unwrapping algorithm [25], and spatially-filtered using sophisticated harmonic artifact reduction for phase data with variable kernel size (V-SHARP) [26,27] implemented in MATLAB (singular value decomposition threshold = 0.05, maximum kernel radius = 13 voxels), to remove background fields. Quantitative susceptibility maps were reconstructed using a modified iterative version of the Fast QSM method described by Li et al. [28], which is based on the thresholded k-space division (TKD) method with threshold larger than 2/3 [29-31] and k-space filtering around the singularity cone surface. A scaling factor for correction of possible underestimation of the quantitative susceptibility values was estimated using a point-spread-function based method [31]. The Fast QSM method has been shown to have good performance in terms of suppressing truncation-related streaking artifacts, but the estimated susceptibility maps may have residual non-local dipole effects [28]. Modifications were therefore made to fit the MR phase/field changes in an iterative way until the residual field is minimum and the fitted susceptibility sources were then superimposed in a way similar to a recently developed QSM method by Wei *et al.* [32]. We refer to this method as the iterative TKD (iTKD) method, and the error tolerance was set to 0.02 in this study. Details of the iTKD algorithm and all empirical parameters can be found in Appendix 1.

A bilateral region was defined in the cortical gray matter (GM) of each rat across five consecutive coronal slices (centered at 0.3 mm from the bregma) using RoiEditor (www.mristudio.org). QSM maps were referenced to the average susceptibility value

measured in this region for each rat. Cortical GM was used as the reference for QSM since it showed no pathology-induced change in the pilocarpine-treated rats as verified by histological assessment. The presence of calcium deposits in the choroid plexus and demyelination in this model precluded the use of ventricular cerebrospinal fluid (CSF) and white matter as reliable references for QSM. For analysis, all brain images were aligned to one control rat brain chosen as the anatomical reference using 6-parameter rigid body registration implemented in Diffeomap (www.mristudio.org). The registration procedure was driven by the intensity of GRE magnitude images, and the resulting transformations were applied to align the susceptibility and R2* maps from each rat.

Subjective qualitative assessment of the susceptibility and R2* maps was performed by one reader (M.A., with 10 years of experience in interpreting rat brain MR images). Thalamic lesions were identified based on their intensity in R2* and susceptibility maps relative to intensities of corresponding regions in the control brains. 34 regions of interest (ROIs) were manually drawn (by M.A.) to include lesioned and non-lesioned areas across the thalami of pilocarpine-treated rats. ROIs were defined in coronal slices of the QSM reconstructed images using RoiEditor (www.mristudio.org), with an average size of 118 ± 31 voxels (mean ± s.d.). The mean susceptibility value in each ROI was calculated by summing the voxel susceptibility values divided by the ROI volume. Corresponding ROIs were identified in Perls'- and Alizarin-stained histological sections at the same coronal levels for optical density (OD) measurements as described below.

Histological processing

Following MRI, the brains were placed in a cryoprotective solution containing 20% glycerol in 0.02 M potassium phosphate-buffered saline (KPBS; pH 7.4) for 36 h, and then frozen in dry ice and stored at −70 °C until cutting. Brains were sectioned into 30-μm thick coronal sections (1:5 series) using a sliding microtome. The first series of sections was stored in 10% formalin at room temperature, and the remaining series in a cryoprotectant tissue-collecting solution (30% ethylene glycol, 25% glycerol in 0.05 M sodium phosphate buffer) at −20°C until processed. From one series, 1-in-2 sections were stained with Alizarin red S to detect accumulation of calcium in the tissue. Sections were mounted on gelatin-coated slides and dried at 37°C. Then, sections were hydrated in descending series of ethanol, rinsed in distilled water, and immersed in 2% Alizarin red S (w/v, distilled water pH 4.1-4.3) (A5533, Sigma-Aldrich) for 45 s. Sections were quickly dehydrated with acetone, acetone:xylene (1:1), and xylene, and then mounted in DePeX. To assess accumulation of iron, 1-in-2 consecutive sections from that series were stained using Perls' method with 3, 3′-diaminobenzidine (DAB) intensification. First, the mounted sections were treated with 1:1 mixture of 2.5% potassium ferrocyanide (#31254, Riel-de Haën, Germany) and 2.5% HCl for 2 h at 37°C, and then washed in PBS three times for 10 min each. Next, the sections were incubated in 0.5 mg/ml DAB (#K4001, Thermo Scientific, USA) for 30 minutes and then immersed in a mixture of 0.5 mg/ml DAB and 0.01% H_2O_2 for 30 min in the dark. Finally, the sections were washed in PBS three times for 10 min each, dehydrated, cleared in xylene, and coverslipped with DePeX. Histological images were subjectively assessed by an independent reader (A.S., with 12 years of experience in analysis of histopathological data). Lesioned tissue areas with iron or calcium deposits were identified as regions that showed

positive staining in Perls' or Alizarin red S-stained sections, respectively, compared to sections from control rat brains.

Optical density measurements

Optical density (OD) of Perls'- and Alizarin red S-stained sections in selected thalamic areas was quantified using the ImageJ software (Fiji ImageJ, version 1.50g). Digital photomicrographs were captured from each stained-section using a Zeiss AxioImager M2 microscope equipped with an AxioCam HRc camera. After conversion of the photomicrographs to grayscale, we obtained intensity values from each ROI (I_{ROI}) of selected thalamic nuclei at the same coronal level as the MR images. Background staining intensity values ($I_{Background}$) were measured in circular ROIs (71 μm^2) placed in three areas with no staining in each photomicrograph, to compensate for any staining differences across sections. OD values from each ROI were extracted by normalizing the measured OD in each ROI to the background intensity values ($OD = (I_{Background} - I_{ROI})/I_{Background}$).

Quantitative analysis

Multiple linear regression was applied to evaluate the association between mean susceptibility measurements referenced to cortical GM ($\Delta\chi$) and the optical densities of iron and calcium in the ROIs, and significance was assessed using the *F*-test with $p < 0.01$ considered statistically significant. In addition to thalamic ROIs, volumes of interest were also identified in major gray and white matter structures in the brain for comparison of quantitative susceptibility values between the control and pilocarpine-treated animal groups. All statistical tests were performed using MATLAB (Mathworks Inc., Natick, MA, USA).

RESULTS

Detection of thalamic lesions with heterogeneous susceptibility contrast

Fig. 1 shows GRE magnitude, R2*, and quantitative susceptibility maps from representative control and pilocarpine-treated rats. R2* maps revealed prominent bilateral lesions in the thalamus of pilocarpine-treated rats, identifiable as areas that appeared significantly ($p < 0.001$) hyperintense compared to corresponding regions in control brains. These hyperintense R2* areas were bilaterally symmetric, and were observed in reproducible dorsal and medial regions of the thalamus in the pilocarpine-treated rats (R2* maps in Fig. 1). In comparison, quantitative susceptibility maps at the same level showed markedly more heterogeneous contrast within the lesions (Fig. 1). Distinct areas within the lesions were found to exhibit significantly ($p < 0.005$) positive (paramagnetic) or negative (diamagnetic) susceptibility values compared with corresponding regions in control brains. Representative susceptibility values measured in paramagnetic and diamagnetic lesion areas shown in Fig. 1 were 0.056 ± 0.017 ppm and -0.031 ± 0.012 ppm relative to cortical GM, respectively (mean ± standard deviation, for QSM hyperintense and hypointense areas outlined in Fig. 1). Comparison of V-SHARP filtered GRE phase/frequency maps and reconstructed susceptibility maps at the same level revealed marked differences in contrast in the lesions (Fig. 2). Poor local correspondence can be observed between hyperintense and hypointense appearance of lesion areas in the phase and susceptibility maps (Fig. 2, arrows).

Fig. 3 compares R2* and susceptibility maps of control and pilocarpine-treated rats with Perls'- and Alizarin red S-stained sections from the same brains. The thalamus of control rats stained negative for both iron and calcium (Fig. 3C, D). In comparison, sections from pilocarpine-treated rats revealed localized deposits of iron- and calcium-positive granules in specific dorsal and medial aspects of the thalamus (Fig. 3G, H), which corresponded closely to paramagnetic and diamagnetic regions delineated in the QSM image (Fig. 3F). In regions where iron and calcium deposits co-localized (Fig. 3G″, H″), relatively positive contrast was observed in the QSM image, indicating local susceptibility shift dominated by iron concentration. High-magnification views of select thalamic regions shown in Fig. 3H′–H″ depict calcium deposits in the form of diffuse microscopic granules, with only a few small formed crystals (indicated by arrowheads in Fig. 3H″).

Representative R2* and quantitative susceptibility maps from pilocarpine-treated rats at the level of the anterior thalamus are depicted in Fig. 4. Bilateral and symmetric hyperintense lesions could be delineated in the anterior thalamus in R2* maps (Fig. 4B, E), with distinct lesion areas appearing relatively diamagnetic and paramagnetic in the QSM images (arrows in Fig. 4C, F). Perls' and Alizarin red S staining of the anterior thalamus revealed very fine iron and calcium deposits localized to the same thalamic areas (Fig. 5). In Fig. 5, a close correspondence can be observed between regional iron deposition revealed by Perls' stain and paramagnetic areas delineated at the periphery of the lesion in the QSM image, and between diffuse calcium deposits and relatively diamagnetic regions in the QSM image. In comparison, these regions could not be effectively differentiated in the R2* map (Fig. 5B).

Fig. 6 shows comparison of QSM and R2* maps of pilocarpine-treated rats with coronal panels from the rat brain atlas by Paxinos and Watson [33]. The bilaterally-symmetric lesioned areas were found to closely follow anatomical boundaries of specific thalamic nuclei along the anterior-posterior brain axis. Major thalamic nuclei that corresponded to the lesioned areas identified in R2* and QSM images included the posterior thalamic nuclei group, the lateral posterior nucleus, lateral geniculate nuclei, and the oval paracentral nucleus (Fig. 6).

Quantitative analysis

Multiple regression analysis indicated a significant relationship between quantitative susceptibility values and histologically-measured optical densities of iron and calcium in the thalamic lesions ($\Delta\chi = -0.006 + 0.58[OD_{iron}] - 0.26[OD_{calcium}]$, $R^2=0.42$, $p<0.001$). The fitted regression coefficient for OD of iron was positive ($p < 0.001$) whereas the regression coefficient for OD of calcium was negative ($p = 0.006$), indicating the specificity of QSM to discriminate between local iron and calcium deposition in the lesions. The results of the regression analysis are plotted in Fig. 7.

Table 1 lists mean susceptibility values measured in major grey and white matter structures in the control and pilocarpine-treated groups. No significant differences in susceptibility were observed between the control and pilocarpine-treated rats for cortical and striatal regions ($p = 0.29$ and 0.79, respectively), and white matter tracts including the optic tract, corpus callosum, and anterior commissure ($p = 0.76$, 0.12 and 0.11, respectively).

DISCUSSION

In this study, we demonstrated the detection of pathological iron and calcium accumulations in specific thalamic nuclei of rats with pilocarpine-induced SE using QSM based on 3D isotropic high-resolution GRE imaging at 11.7 T. Quantitative susceptibility maps provided high spatial accuracy to enable detection and differentiation of localized deposits of iron and calcium compared to R2* and GRE phase images, as validated by histological assessment of the same brains. Notably, the results of this study showed the detection of early-stage, amorphous calcium salt deposits present in the form of diffuse and small granules in the thalamus, which are different from fully formed calcifications observed in later stages of the disease. These findings demonstrate the potential of QSM to detect subtle pathological changes in tissue composition after SE, and indicate that QSM may provide a promising technique for diagnosis and characterization of thalamic lesions after SE.

A linear correlation between R2* and quantitative susceptibility values has been demonstrated in studies examining pathological and age-related iron accumulation in the brain [34]. In pathological brain lesions with varying degrees of calcification, however, R2* does not exhibit a linear or monotonic relationship with magnetic susceptibility. In pilocarpine-treated rats, R2* maps exhibited hyperintensity for both iron- and calcium-containing lesion areas, and offered no discriminative power to distinguish between these deposits or provide information about lesion composition. As R2* reflects the effect of net intravoxel spin dephasing, it does not provide differential sensitivity to dephasing induced by paramagnetic or diamagnetic sources of field perturbation. In turn, quantitative susceptibility maps showed lesion contrasts that were more consistent with the tissue changes observed in histological sections. Furthermore, quantitative analysis showed a significant positive dependence of susceptibility measurements on OD of Perls' staining (iron), and a significant negative dependence on OD of Alizarin red S staining (calcium). These findings indicate that QSM can provide improved spatial accuracy and greater diagnostic value in the classification of thalamic lesions following SE.

Calcium salt deposits in brain parenchyma are composed of calcium phosphate in the form of hydroxyapatite, which has been reported to have a volume susceptibility of −14.83 ppm [35], making it slightly diamagnetic relative to water. At our experimental time point, calcium deposits were found in the form of diffuse microscopic granules, with only a few small formed crystals. These diffuse granular deposits are distinct from fully-formed calcifications that are observed in more advanced stages of the disease [23]. It has been demonstrated that granular deposits increase in size and concentration over time to form calcified aggregates [5], which may be an indicator of the maturity of the lesion, and consequently, the time from the initial injury. Our data demonstrate the sensitivity of QSM to detect these early-stage diffuse deposits of calcium, which could yield a useful surrogate marker to examine progressive calcification in thalamic lesions.

Thalamic iron accumulation in pilocarpine-treated rats corresponding to the hyperintense lesion areas detected in susceptibility maps was observed in the form of fine and diffuse deposits in Perls'-stained sections, as opposed to localized and condensed iron deposits reported in intracerebral hemorrhages. We hypothesize that the pathological accumulation of

iron in the thalamus after SE may stem from two sources; first is the disruption of the blood-brain barrier (BBB), and second from physiological iron accompanying microglia/macrophage activation. BBB leakage has been reported in both human epilepsy and in animal models of SE [36]. Spatially, BBB permeability reported in a recent study [37] also appears to overlap with the location and extent of bilateral thalamic lesions observed in our study. The second source of iron deposition may arise from iron-positive microglia/macrophages, which contain iron in the form of hemosiderin, and are also thought to contribute to the calcification process [4]. The accumulation of iron in the present study coincided with areas of localized gliosis as assessed with Nissl-stained sections (not shown), further supporting the notion that glial activation may contribute to iron deposition and resulting paramagnetic contrast observed in the susceptibility maps. Deciphering whether the iron contributing to the paramagnetic contrast in susceptibility maps after pilocarpine-induced SE is systemic iron or cerebral iron or both, however, warrants further investigation.

Our data also demonstrate caveats in the interpretation of GRE phase or frequency contrast for characterizing brain tissue lesions. GRE phase imaging and SWI have been shown to be useful for differentiating intracranial calcifications and hemorrhages [38-40]. In the present study, background-corrected phase and reconstructed susceptibility maps were found to exhibit significant differences in contrast in the areas with thalamic lesions. These findings are consistent with recent reports in the human brain [21,22,41]. Furthermore, comparison of the MRI data with Perls' and Alizarin red S stainings showed that compared to QSM, phase maps did not reliably distinguish between areas with local iron and calcium deposits. These results can be ascribed to the known non-local nature of the GRE signal phase. Measured phase reflects a non-local convolution of the underlying magnetic susceptibility distribution, and is thus subject to contributions from perturbers outside the imaging voxel. Moreover, GRE signal phase is dependent on acquisition parameters (particularly TE), lesion shape and orientation with respect to the main magnetic field [26,42], and contrast in phase maps can also be affected by the spatial filtering method applied [43]. Therefore, lesion contrast in phase maps needs to be interpreted with caution, and can lead to misclassification of paramagnetic and diamagnetic areas.

At the experimental time point examined in this study, co-localization of iron and calcium deposits was observed in several thalamic lesions, although calcium deposition extended to areas with no iron accumulation. This is in agreement with previous reports describing that the accumulation of iron tends to precede the deposition of calcium and other minerals in cerebral lesions [24]. In areas where iron and calcium co-localized, the susceptibility maps exhibited hyperintensity, which can be attributed to the dominant paramagnetic susceptibility shift induced by iron. Further longitudinal studies are necessary to evaluate changes in magnetic susceptibility and the spatial distribution of paramagnetic and diamagnetic lesion areas with progressive calcification and maturity of the lesions after injury.

In our study, bilateral and symmetric lesions were detected in R2* and susceptibility maps in reproducible thalamic areas in the pilocarpine-treated group. Limited data are available in the literature on the role of thalamic nuclei in epileptogenesis following SE. A few previous studies in epilepsy patients have also reported hyperintense T2-weighted lesions in the thalamus, mostly in the pulvinar region [44]. To our knowledge, this is the first study to

show that thalamic lesions in the rat brain following pilocarpine-induced SE are nuclei-specific, and correspond closely to anatomical boundaries of particular thalamic nuclei across animals. While the pathological mechanisms underlying the nuclei-specificity of lesions observed in our study are not clear, this could indicate the selective involvement of these thalamic nuclei in epileptogenesis after pilocarpine-induced SE.

We did not observe significant variations in $\Delta\chi$ in different gray and white matter anatomical structures between the pilocarpine-treated and control rats, although mean susceptibility values were slightly lower in the pilocarpine-treated group in major white matter tracts examined. While our results indicate that there are no significant pathology-induced changes in magnetic susceptibility in these structures in the pilocarpine model of SE, the relatively small sample size in our study and inter-subject variance could also affect the sensitivity of statistical group comparison to detect susceptibility differences due to potential white matter pathology.

It is also necessary to note the limitations of this study. While our study showed a significant correlation between $\Delta\chi$ measurements in the lesions and the optical densities of iron- and calcium-specific stains, sources contributing to susceptibility variation in pathological lesions are manifold, and include myelin, demyelination, and presence of trace elements such as copper, zinc etc., which also exert paramagnetic/diamagnetic effects. Susceptibility contrast in the thalamus can be affected by myelin content [45]. However, due to the TE-dependent and anisotropic effect of myelinated fibers and white matter microstructure on measured susceptibility [46,47], histological correlation with myelin staining is not straightforward. Further, focal mineralization in the lesions can be accompanied by varying degrees of demyelination, thus the contribution of myelin to QSM contrast in thalamic grey matter nuclei is expected to be weak in comparison to the effects of pathological iron and calcium accumulations. It is also necessary to note that the regression analysis in our study was performed on measured ODs of histological Perls' and Alizarin red S stainings. Standards to assess absolute iron and calcium concentrations are not readily available for the analysis of Perls'- and Alizarin red S-stained material, therefore only relative quantities of iron and calcium deposition across lesions can be measured. Future studies using mass spectrometry may enable more robust quantification of iron and calcium concentrations in the lesions and their comparison with QSM contrast.

In the present study, the iTKD method was applied for QSM reconstruction without use of regularization or *a priori* constraints, to best preserve the contrast around small thalamic lesions as well as anatomical structures in the rat brain while achieving minimization of streaking artifacts [28]. Current QSM techniques, however, still have some known limitations, and reconstructed susceptibility maps can have effects from residual background field contributions and confounding artifacts particularly in voxels adjacent to blood vessels and areas adjoining tissue-air interface. Further technical advances with more sophisticated QSM reconstruction methods may enable improved accuracy of lesion detection and delineation in the epileptogenic brain.

In conclusion, the results of this study demonstrate that QSM can enable detection and differentiation of pathological thalamic nuclei-specific deposits of iron and calcium with

high sensitivity and improved spatial accuracy compared to R2* or GRE phase imaging. QSM may thus become an important technique to investigate localized changes in tissue composition and progressive calcification in thalamic lesions following SE in experimental models and in the clinic.

Acknowledgments

This work was supported by NIH grants R03EB017806 and R21NS096249 (to M.A.), and Academy of Finland (O.G., A.S.). Part of X.L.'s salary was supported by NIH/NIBIB P41EB015909. The authors thank Ms. Maarit Pulkkinen for technical assistance with histological preparations.

Appendix 1

The iTKD method is a modified iterative version of the fast QSM method as described in Li et al. [28]. The fast QSM method consists of three steps to estimate the tissue susceptibility sources from the relative magnetic field shift δB or normalized phase ψ as in [28], with good performance in terms of streaking artifacts suppression. The three steps can be described in Eqs. (A1–A3),

$$\chi_{1k}=c_{\chi}^{-1}\cdot sign\left(D_2\right)\cdot\delta B_k \quad \text{(A1)}$$

$$\chi_{2k}=\chi_{1k}\cdot W_{FS}+LPF\left(\chi_{1k}\right)\cdot\left(1-W_{FS}\right) \quad \text{(A2)}$$

$$\chi_3=FT^{-1}\{FT\left(M\cdot\chi_2\right)\cdot W_{FS}+LPF[FT\left(M\cdot\chi_2\right)]\cdot\left(1-W_{FS}\right)\}\cdot M \quad \text{(A3)}$$

where the subscript k indicates a variable in k-space, i.e. $\delta B_k=FT\left(\delta B\right)$ with FT indicating the Fourier transform; D_2 is the well known susceptibility to field kernel, i.e. $D_2=\frac{1}{3}-\frac{\left(\hat{\boldsymbol{H}}\cdot\boldsymbol{k}\right)^2}{k^2}$, with $\hat{\boldsymbol{H}}$ being the main field direction and $\boldsymbol{k}$ the spatial frequency vector; $sign$ is the signum function, and $c_{\chi}=p\left(2/3,0\right)$ is a scaling factor for correcting the systematic underestimation due to kernel modification similar to Eqs. (6–8) in [31], with $p\left(2/3,\boldsymbol{r}\right)=FT^{-1}\left(D_2\cdot sign\left(D_2\right)\right)$. In the present study, the low-pass filter (LPF) in Eq. (A2–A3) was a spherical mean value filter with radius of 3 voxels and the weighting function W_{FS} in Fourier space was defined as $W_{FS}=\begin{cases}0, & W_0<0\\ W_0, & 0<W_0<1\\ 1, & W_0>1\end{cases}$ where $W_0=\left(|D_2|-a\right)/\left(b-a\right)$, with a,b being the 1st and 30th percentile values of $|D_2|$, respectively. M in (A3) is a binary brain mask. In order to minimize the residual non-local effect in the susceptibility maps obtained by the fast QSM method as reported in [28], modification was made in the iTKD method by iteratively fitting the residual local field shift

$\delta B_r = M \cdot \left(\delta B - FT^{-1}\left(FT\left(\chi_{iTKD\_i}\right) \cdot D_2\right)\right)$ using the same fast QSM method to obtain the residual susceptibility source $\Delta\chi$ and then superimposing such sources to the susceptibility maps i.e. $\Delta\chi = fastQSM\left(\delta B_r\right)$; $\chi_{iTKD\_i+1} = \chi_{iTKD\_i} + \Delta\chi$. This iteration was set to stop if $\|\delta B_r\| / \|\delta B\|$ or $\|\Delta\chi\| / \|\chi_{iTKD\_i+1}\|$ is less then the set tolerance (0.02 used in this study).

References

1. Herman ST. Epilepsy after brain insult: targeting epileptogenesis. Neurology. 2002; 59(9 Suppl 5):S21–26.
2. Pitkanen A, Kharatishvili I, Karhunen H, Lukasiuk K, Immonen R, Nairismagi J, Grohn O, Nissinen J. Epileptogenesis in experimental models. Epilepsia. 2007; 48(Suppl 2):13–20.
3. Loscher W. Critical review of current animal models of seizures and epilepsy used in the discovery and development of new antiepileptic drugs. Seizure. 2011; 20(5):359–368. [PubMed: 21292505]
4. Gayoso MJ, Al-Majdalawi A, Garrosa M, Calvo B, Diaz-Flores L. Selective calcification of rat brain lesions caused by systemic administration of kainic acid. Histol Histopathol. 2003; 18(3):855–869. [PubMed: 12792898]
5. Lafreniere GF, Peredery O, Persinger MA. Progressive accumulation of large aggregates of calcium-containing polysaccharides and basophilic debris within specific thalamic nuclei after lithium/pilocarpine-induced seizures. Brain Res Bull. 1992; 28(5):825–830. [PubMed: 1377589]
6. Casanova MF, Araque JM. Mineralization of the basal ganglia: implications for neuropsychiatry, pathology and neuroimaging. Psychiatry Res. 2003; 121(1):59–87. [PubMed: 14572624]
7. Kim KM. Apoptosis and calcification. Scanning Microsc. 1995; 9(4):1137–1175. discussion 1175–11380. [PubMed: 8819895]
8. Wang Y, Liu T. Quantitative susceptibility mapping (QSM): Decoding MRI data for a tissue magnetic biomarker. Magn Reson Med. 2015; 73(1):82–101. [PubMed: 25044035]
9. Haacke EM, Liu S, Buch S, Zheng W, Wu D, Ye Y. Quantitative susceptibility mapping: current status and future directions. Magn Reson Imaging. 2015; 33(1):1–25. [PubMed: 25267705]
10. Liu C, Wei H, Gong NJ, Cronin M, Dibb R, Decker K. Quantitative Susceptibility Mapping: Contrast Mechanisms and Clinical Applications. Tomography. 2015; 1(1):3–17. [PubMed: 26844301]
11. Schweser F, Deistung A, Lehr BW, Reichenbach JR. Differentiation between diamagnetic and paramagnetic cerebral lesions based on magnetic susceptibility mapping. Med Phys. 2010; 37(10): 5165–5178. [PubMed: 21089750]
12. Wu Z, Mittal S, Kish K, Yu Y, Hu J, Haacke EM. Identification of calcification with MRI using susceptibility-weighted imaging: a case study. J Magn Reson Imaging. 2009; 29(1):177–182. [PubMed: 19097156]
13. Yamada N, Imakita S, Sakuma T, Takamiya M. Intracranial calcification on gradient-echo phase image: depiction of diamagnetic susceptibility. Radiology. 1996; 198(1):171–178. [PubMed: 8539373]
14. Klohs J, Deistung A, Schweser F, Grandjean J, Dominietto M, Waschkies C, Nitsch RM, Knuesel I, Reichenbach JR, Rudin M. Detection of cerebral microbleeds with quantitative susceptibility mapping in the ArcAbeta mouse model of cerebral amyloidosis. J Cereb Blood Flow Metab. 2011; 31(12):2282–2292. [PubMed: 21847134]
15. Liu T, Surapaneni K, Lou M, Cheng L, Spincemaille P, Wang Y. Cerebral microbleeds: burden assessment by using quantitative susceptibility mapping. Radiology. 2012; 262(1):269–278. [PubMed: 22056688]
16. Bilgic B, Pfefferbaum A, Rohlfing T, Sullivan EV, Adalsteinsson E. MRI estimates of brain iron concentration in normal aging using quantitative susceptibility mapping. Neuroimage. 2012; 59(3): 2625–2635. [PubMed: 21925274]
17. Langkammer C, Schweser F, Krebs N, Deistung A, Goessler W, Scheurer E, Sommer K, Reishofer G, Yen K, Fazekas F, Ropele S, Reichenbach JR. Quantitative susceptibility mapping (QSM) as a

means to measure brain iron? A post mortem validation study. Neuroimage. 2012; 62(3):1593–1599. [PubMed: 22634862]

18. Zheng W, Nichol H, Liu S, Cheng YC, Haacke EM. Measuring iron in the brain using quantitative susceptibility mapping and X-ray fluorescence imaging. Neuroimage. 2013; 78:68–74. [PubMed: 23591072]
19. Lotfipour AK, Wharton S, Schwarz ST, Gontu V, Schafer A, Peters AM, Bowtell RW, Auer DP, Gowland PA, Bajaj NP. High resolution magnetic susceptibility mapping of the substantia nigra in Parkinson's disease. J Magn Reson Imaging. 2012; 35(1):48–55. [PubMed: 21987471]
20. Wisnieff C, Ramanan S, Olesik J, Gauthier S, Wang Y, Pitt D. Quantitative susceptibility mapping (QSM) of white matter multiple sclerosis lesions: Interpreting positive susceptibility and the presence of iron. Magn Reson Med. 2015; 74(2):564–570. [PubMed: 25137340]
21. Chen W, Zhu W, Kovanlikaya I, Kovanlikaya A, Liu T, Wang S, Salustri C, Wang Y. Intracranial calcifications and hemorrhages: characterization with quantitative susceptibility mapping. Radiology. 2014; 270(2):496–505. [PubMed: 24126366]
22. Deistung A, Schweser F, Wiestler B, Abello M, Roethke M, Sahm F, Wick W, Nagel AM, Heiland S, Schlemmer HP, Bendszus M, Reichenbach JR, Radbruch A. Quantitative susceptibility mapping differentiates between blood depositions and calcifications in patients with glioblastoma. PLoS One. 2013; 8(3):e57924. [PubMed: 23555565]
23. Lehto LJ, Sierra A, Corum CA, Zhang J, Idiyatullin D, Pitkanen A, Garwood M, Grohn O. Detection of calcifications in vivo and ex vivo after brain injury in rat using SWIFT. Neuroimage. 2012; 61(4):761–772. [PubMed: 22425671]
24. Harder SL, Hopp KM, Ward H, Neglio H, Gitlin J, Kido D. Mineralization of the deep gray matter with age: a retrospective review with susceptibility-weighted MR imaging. AJNR Am J Neuroradiol. 2008; 29(1):176–183. [PubMed: 17989376]
25. Li W, Wu B, Liu C. Quantitative susceptibility mapping of human brain reflects spatial variation in tissue composition. Neuroimage. 2011; 55(4):1645–1656. [PubMed: 21224002]
26. Schweser F, Deistung A, Lehr BW, Reichenbach JR. Quantitative imaging of intrinsic magnetic tissue properties using MRI signal phase: an approach to in vivo brain iron metabolism? Neuroimage. 2011; 54(4):2789–2807. [PubMed: 21040794]
27. Wu B, Li W, Guidon A, Liu C. Whole brain susceptibility mapping using compressed sensing. Magn Reson Med. 2012; 67(1):137–147. [PubMed: 21671269]
28. Li W, Wang N, Yu F, Han H, Cao W, Romero R, Tantiwongkosi B, Duong TQ, Liu C. A method for estimating and removing streaking artifacts in quantitative susceptibility mapping. Neuroimage. 2015; 108:111–122. [PubMed: 25536496]
29. Wharton S, Bowtell R. Whole-brain susceptibility mapping at high field: a comparison of multiple- and single-orientation methods. Neuroimage. 2010; 53(2):515–525. [PubMed: 20615474]
30. Shmueli K, de Zwart JA, van Gelderen P, Li TQ, Dodd SJ, Duyn JH. Magnetic susceptibility mapping of brain tissue in vivo using MRI phase data. Magn Reson Med. 2009; 62(6):1510–1522. [PubMed: 19859937]
31. Schweser F, Deistung A, Sommer K, Reichenbach JR. Toward online reconstruction of quantitative susceptibility maps: superfast dipole inversion. Magn Reson Med. 2013; 69(6):1582–1594. [PubMed: 22791625]
32. Wei H, Dibb R, Zhou Y, Sun Y, Xu J, Wang N, Liu C. Streaking artifact reduction for quantitative susceptibility mapping of sources with large dynamic range. NMR Biomed. 2015; 28(10):1294–1303. [PubMed: 26313885]
33. Paxinos, G., Watson, C. The Rat Brain in Stereotaxic Coordinates. Academic Press; 2004.
34. Tan H, Liu T, Wu Y, Thacker J, Shenkar R, Mikati AG, Shi C, Dykstra C, Wang Y, Prasad PV, Edelman RR, Awad IA. Evaluation of iron content in human cerebral cavernous malformation using quantitative susceptibility mapping. Invest Radiol. 2014; 49(7):498–504. [PubMed: 24619210]
35. Hopkins JA, Wehrli FW. Magnetic susceptibility measurement of insoluble solids by NMR: magnetic susceptibility of bone. Magn Reson Med. 1997; 37(4):494–500. [PubMed: 9094070]

36. van Vliet EA, da Costa Araujo S, Redeker S, van Schaik R, Aronica E, Gorter JA. Blood-brain barrier leakage may lead to progression of temporal lobe epilepsy. Brain. 2007; 130(Pt 2):521–534. [PubMed: 17124188]
37. Breuer H, Meier M, Schneefeld S, Hartig W, Wittneben A, Markel M, Ross TL, Bengel FM, Bankstahl M, Bankstahl JP. Multimodality imaging of blood-brain barrier impairment during epileptogenesis. J Cereb Blood Flow Metab. 2016
38. Berberat J, Grobholz R, Boxheimer L, Rogers S, Remonda L, Roelcke U. Differentiation between calcification and hemorrhage in brain tumors using susceptibility-weighted imaging: a pilot study. AJR Am J Roentgenol. 2014; 202(4):847–850. [PubMed: 24660715]
39. Gupta RK, Rao SB, Jain R, Pal L, Kumar R, Venkatesh SK, Rathore RK. Differentiation of calcification from chronic hemorrhage with corrected gradient echo phase imaging. J Comput Assist Tomogr. 2001; 25(5):698–704. [PubMed: 11584228]
40. Gronemeyer SA, Langston JW, Hanna SL, Langston JW Jr. MR imaging detection of calcified intracranial lesions and differentiation from iron-laden lesions. J Magn Reson Imaging. 1992; 2(3): 271–276. [PubMed: 1627861]
41. Li X, Harrison DM, Liu H, Jones CK, Oh J, Calabresi PA, van Zijl PC. Magnetic susceptibility contrast variations in multiple sclerosis lesions. J Magn Reson Imaging. 2016; 43(2):463–473. [PubMed: 26073973]
42. Schafer A, Wharton S, Gowland P, Bowtell R. Using magnetic field simulation to study susceptibility-related phase contrast in gradient echo MRI. Neuroimage. 2009; 48(1):126–137. [PubMed: 19520176]
43. Cronin MJ, Wharton S, Al-Radaideh A, Constantinescu C, Evangelou N, Bowtell R, Gowland PA. A comparison of phase imaging and quantitative susceptibility mapping in the imaging of multiple sclerosis lesions at ultrahigh field. MAGMA. 2016; 29(3):543–557. [PubMed: 27112155]
44. Szabo K, Poepel A, Pohlmann-Eden B, Hirsch J, Back T, Sedlaczek O, Hennerici M, Gass A. Diffusion-weighted and perfusion MRI demonstrates parenchymal changes in complex partial status epilepticus. Brain. 2005; 128(Pt 6):1369–1376. [PubMed: 15743871]
45. Deistung A, Schafer A, Schweser F, Biedermann U, Turner R, Reichenbach JR. Toward in vivo histology: a comparison of quantitative susceptibility mapping (QSM) with magnitude-, phase-, and R2*-imaging at ultra-high magnetic field strength. Neuroimage. 2013; 65:299–314. [PubMed: 23036448]
46. Wharton S, Bowtell R. Effects of white matter microstructure on phase and susceptibility maps. Magn Reson Med. 2015; 73(3):1258–1269. [PubMed: 24619643]
47. Aggarwal M, Kageyama Y, Li X, van Zijl PC. B_0-orientation dependent magnetic susceptibility-induced white matter contrast in the human brainstem at 11.7T. Magn Reson Med. 2016; 75(6): 2455–2463. [PubMed: 27018784]

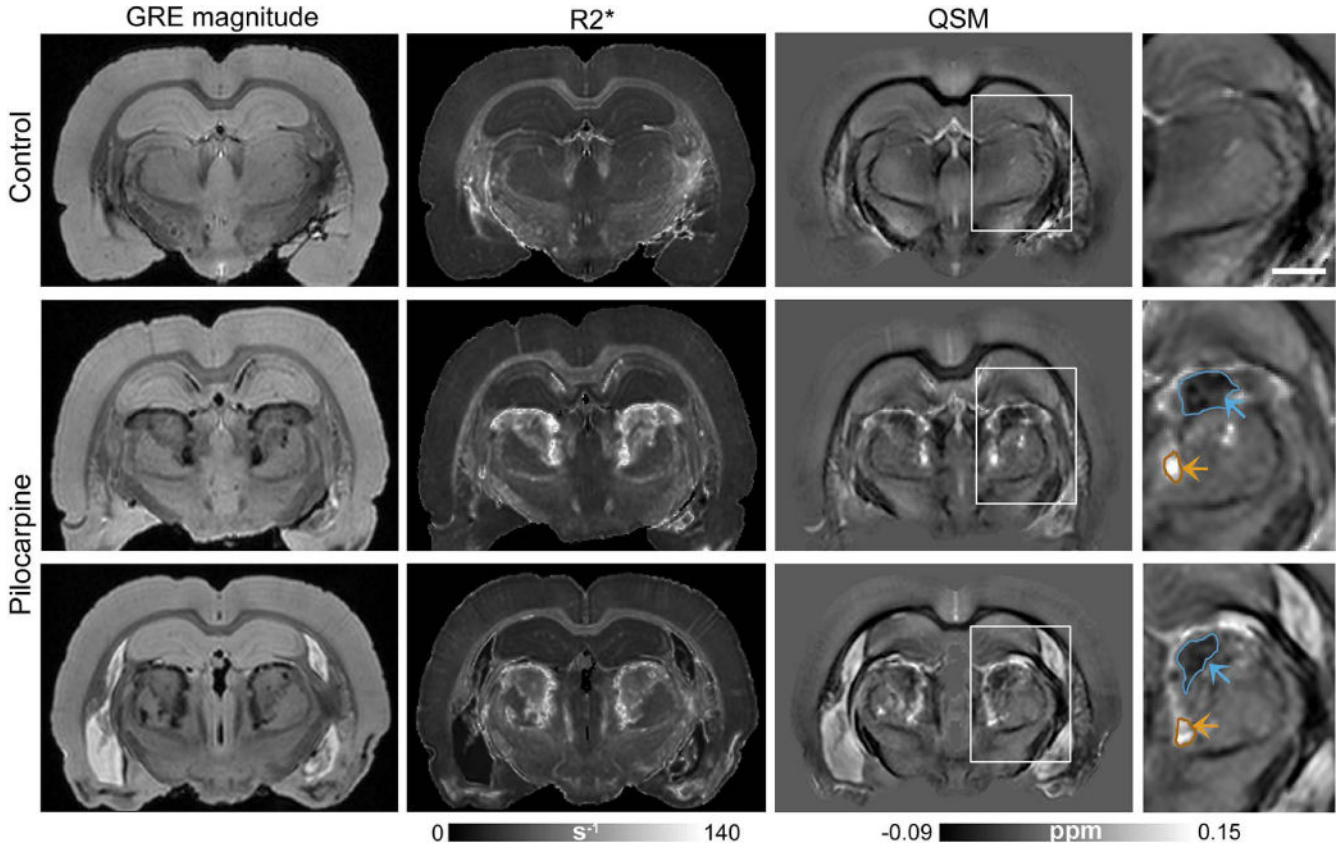

Figure 1.

Bilaterally-symmetric lesions in the thalamus of pilocarpine-treated rats delineated with GRE imaging. Coronal GRE magnitude (TE=15 ms), R2*, and quantitative susceptibility maps from a control rat (top row) and two representative pilocarpine-treated rats (middle, bottom rows) are shown. Bilateral thalamic lesions can be identified as hyperintense areas in the R2* maps. Magnified views of quantitative susceptibility maps in the right panel (corresponding to regions indicated by the white boxes) demonstrate distinct diamagnetic (blue arrows) and paramagnetic (orange arrows) areas delineated within the thalamic lesions. Scale bar: 1.5 mm.

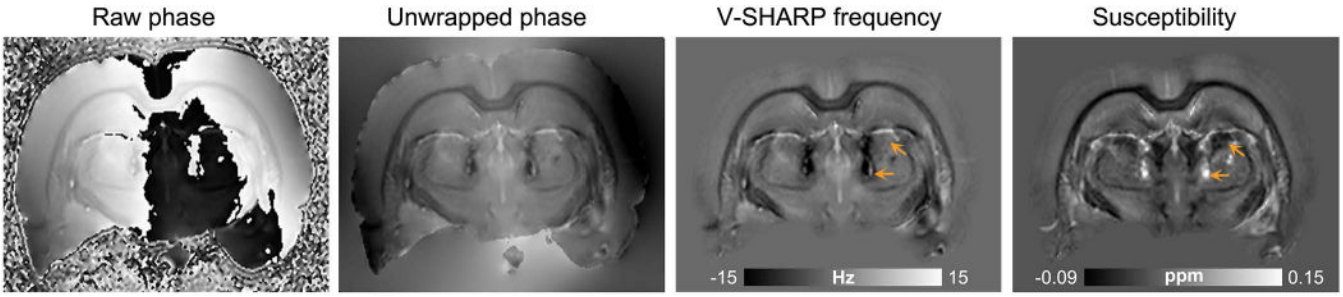

Figure 2.

Comparison of GRE frequency and quantitative susceptibility contrasts in thalamic lesions. A coronal slice from a representative pilocarpine-treated rat brain at the level of thalamic lesions shows the raw GRE phase, unwrapped phase, V-SHARP filtered frequency, and quantitative susceptibility maps. Arrows indicate localized differences in hypointense and hyperintense appearance of lesion areas seen in the frequency and susceptibility maps.

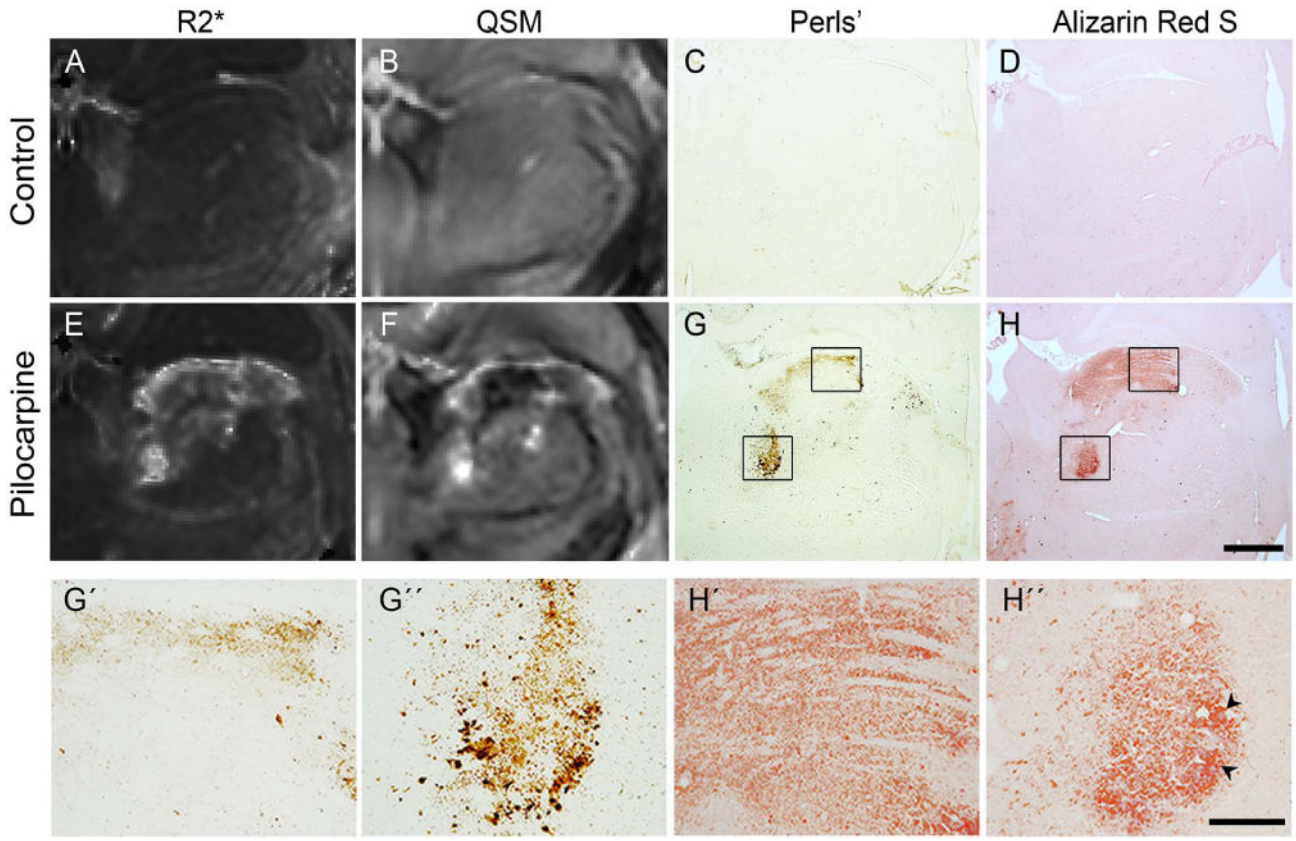

Figure 3.

Comparison of R2* and quantitative susceptibility maps through the thalamus of control (A, B) and pilocarpine-treated (E, F) rats with coronal Perls' (iron) and Alizarin red S (calcium) stained sections from the same brains. Localized deposits of iron and calcium are seen in the pilocarpine-treated rat brain (G, H), which correspond closely to the paramagnetic and diamagnetic regions delineated in the susceptibility map (F). High-magnification views in panels G'-H' and G"-H" (corresponding to areas within the black boxes in G, H) reveal microscopic granular iron and calcium deposits in select thalamic areas, with a few formed calcified crystals (black arrowheads). Scale bar for A-H: 1 mm, scale bar for G'-H": 200 μm.

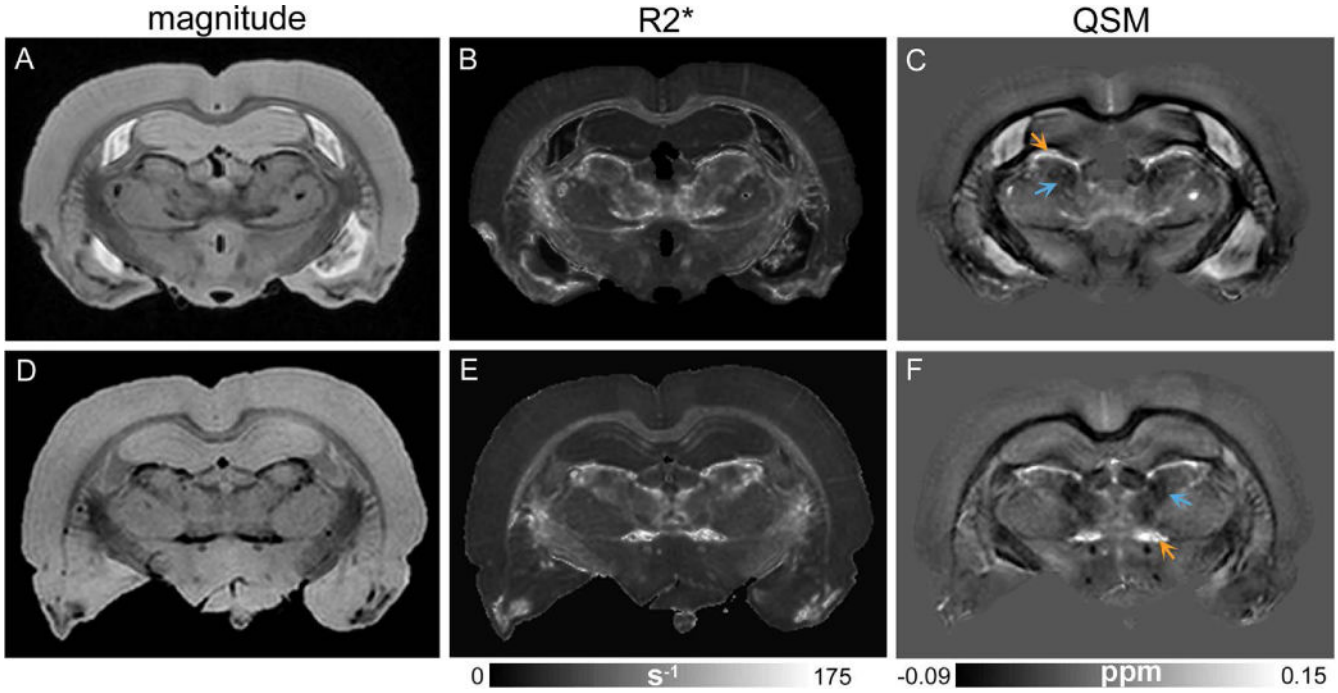

Figure 4.

Delineation of bilateral lesions in the anterior thalamus of pilocarpine-injected rats. Coronal GRE magnitude (A, D), R2* (B, E), and quantitative susceptibility (C, F) maps from two representative pilocarpine-treated rat brains at the level of the anterior thalamus are shown in the top and bottom rows, respectively. Thalamic lesions can be identified as bilateral hypointense and hyperintense areas in the magnitude and R2* images, respectively. Quantitative susceptibility maps (C, F) show heterogeneous contrast within the thalamic lesions, with relatively diamagnetic (blue arrows) and paramagnetic (orange arrows) appearance of distinct lesion areas.

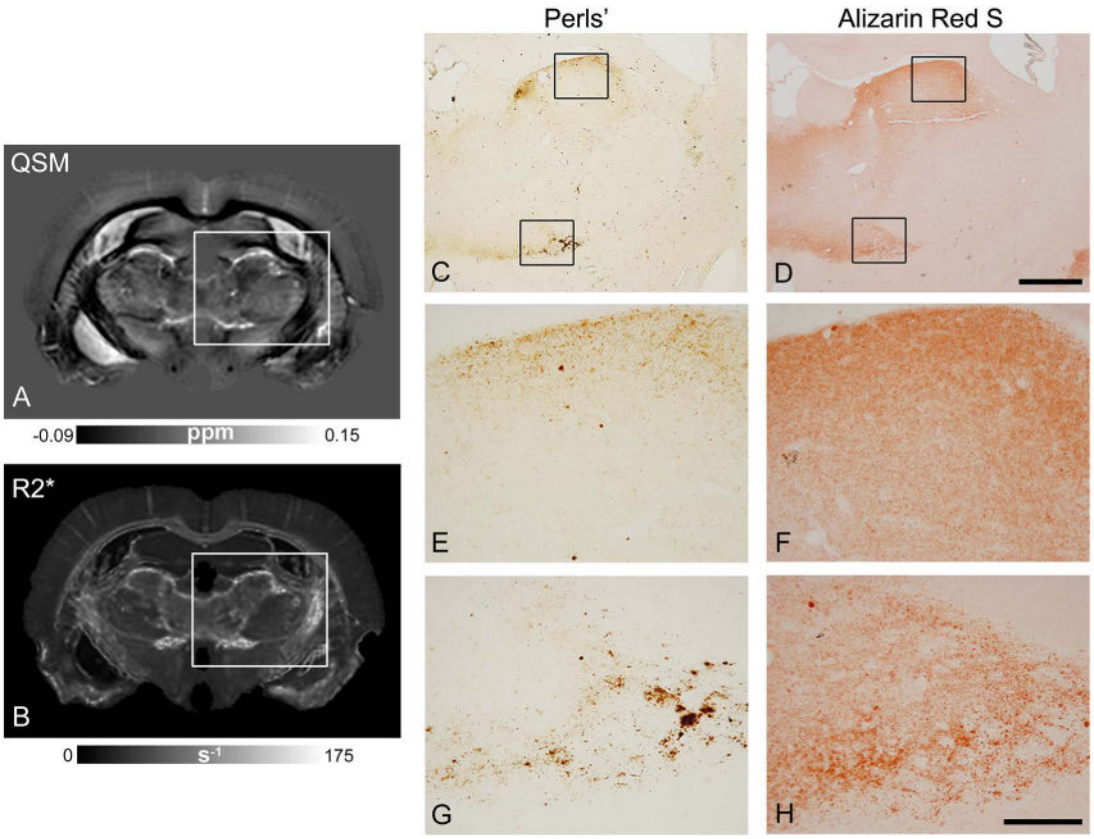

Figure 5.

Comparison of susceptibility and R2* maps with histological Perls'- and Alizarin red S-stained sections from the anterior thalamus of a pilocarpine-treated rat. A-B) Coronal slice from quantitative susceptibility (A) and R2* (B) maps. C-D) Perls's and Alizarin red S stained sections from the same brain show regional deposition of iron and calcium in corresponding thalamic areas. E-H) High-magnification views of histological sections (corresponding to regions indicated by the black boxes in panels C and D) demonstrate diffuse granular deposits of iron and calcium observed in the tissue. Scale bar for C-D: 1 mm, scale bar for E-H: 200 μm.

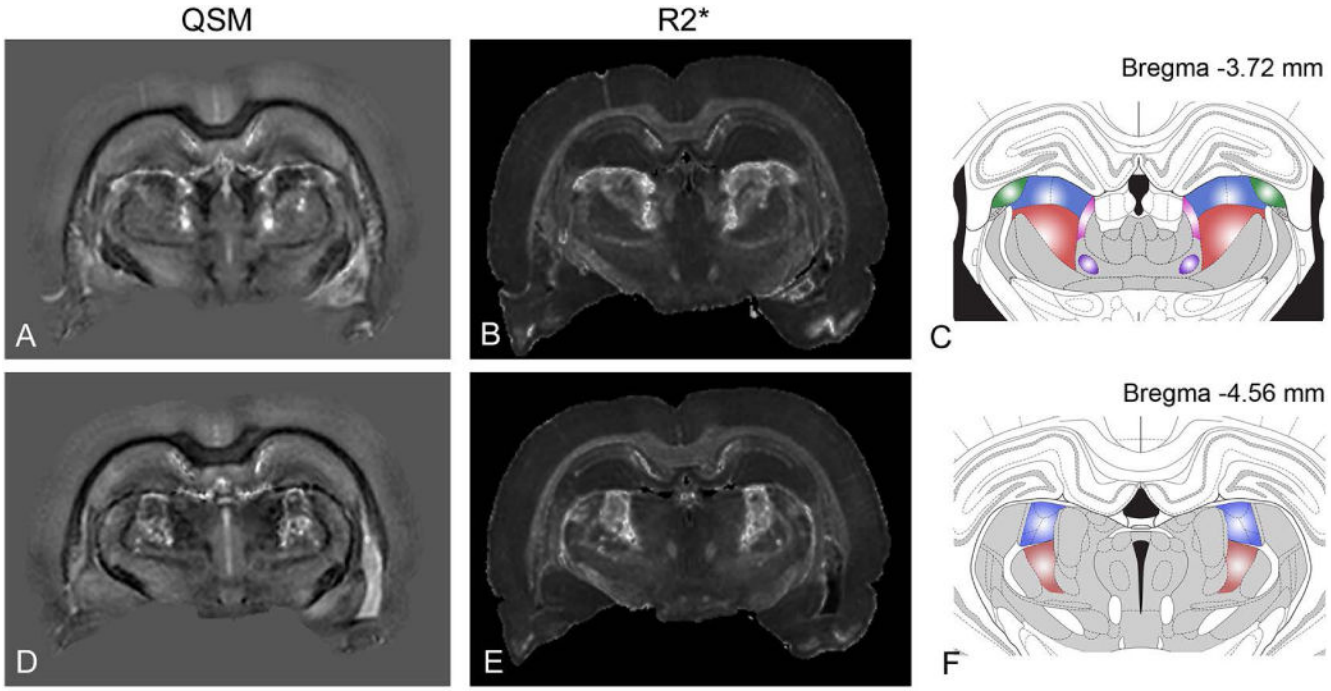

Figure 6.

Nuclei-specificity of thalamic lesions in the rat brain with pilocarpine-induced SE. QSM (A, D) and R2* (B, E) maps at two different coronal levels are compared with corresponding sections from the rat brain atlas (C, F) by Paxinos and Watson (2004). Major thalamic nuclei corresponding to the lesioned areas include: the lateral posterior nucleus (blue), dorsal lateral geniculate nucleus (green), posterior thalamic nuclear group (red), and the oval paracentral nucleus (purple).

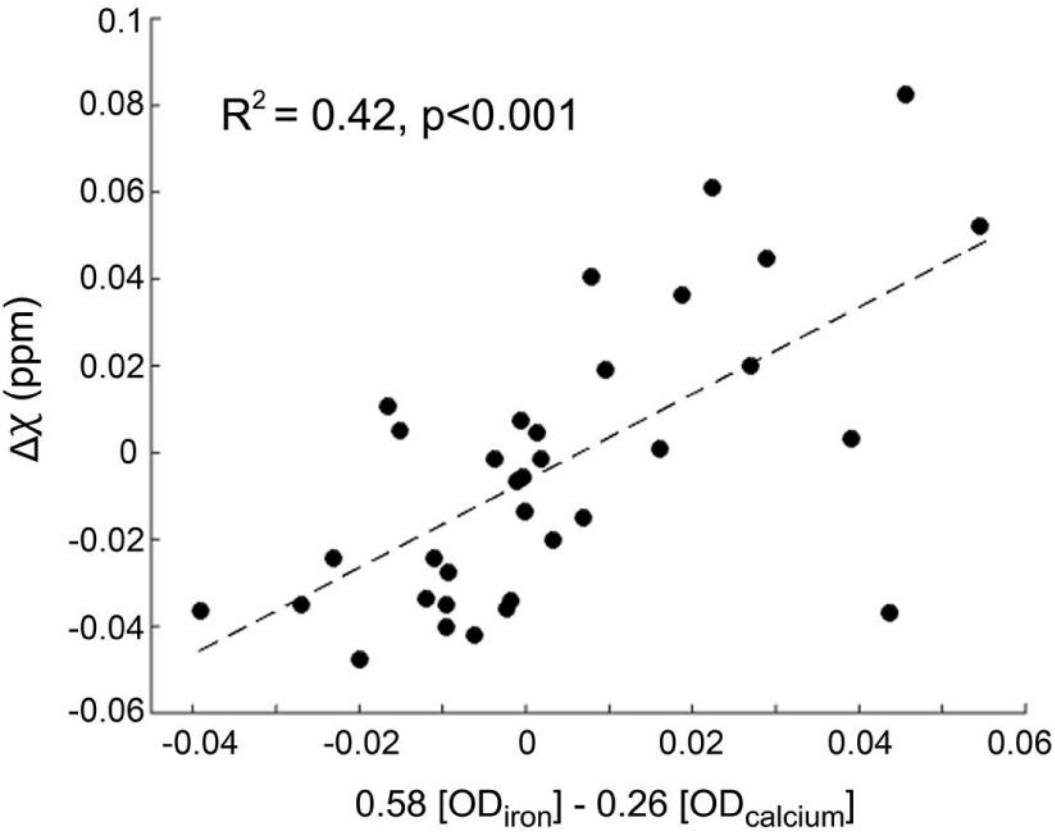

Figure 7.

Plot showing results of multiple regression analysis between susceptibility values (Δχ, referenced to cortical gray matter) and optical densities of iron and calcium in the thalamic lesions as measured from Perls'- and Alizarin red S-stained sections, respectively.

Table 1

Susceptibility values in major gray and white matter structures measured in the control and pilocarpine-treated brains

Brain region	Control	Pilocarpine	p-value
Sensory cortex	−0.42 ± 0.19	−0.66 ± 0.45	0.29
Striatum	−0.96 ± 0.18	−0.97 ± 0.19	0.79
Optic tract	−6.18 ± 0.82	−5.97 ± 1.28	0.76
Corpus callosum	−5.08 ± 0.31	−4.50 ± 0.69	0.12
Anterior commissure	−5.99 ± 0.28	−5.14 ± 1.08	0.11

Values are mean ± s.d. (10^{-2} ppm) referenced to anterior cortical GM, for n=5 rats in each group